1   Revision 1, Manuscript 5528R

2   High-Pressure Compressibility and Thermal Expansion of aragonite

3   Sarah E.M. Palaich[1], Robert A. Heffern[1], Michael Hanfland[2], Andrea Lausi[3], Abby

4   Kavner[1], Craig E. Manning[1], Marco Merlini[4]

5   [1]Department of Earth, Planetary and Space Sciences, University of California, Los

6   Angeles, CA 90095

7   [2]ESRF - The European Synchrotron. 71, avenue des Martyrs, 38000 Grenoble.

8   [3]Elettra - Sincrotrone Trieste S.C.p.A., S.S. 14 km 163,5 in AREA Science Park - loc.

9   Basovizza, 34149 Trieste, Italy

10 [4]Dipartimento di Scienze della Terra, Università degli Studi di Milano. Via Botticelli 23,

11 20133 Milano, Italy

12 **Abstract**

13 The structure and isothermal equation of state of aragonite were determined to 40 GPa

14 using synchrotron single crystal X-ray techniques. In addition, powder diffraction

15 techniques were used to determine thermal expansion between 298-673 K. At room

16 temperature, aragonite has orthorhombic Pnma structure to 40 GPa, with an isothermal

17 bulk modulus of 66.5(7) GPa and K' = 5.0(1). Between 25-30 GPa the aragonite unit cell

18 begins to distort due to a stiffening of the c-axis compressibility, which is controlled by

19 the orientation and distortion of the carbonate groups.   The ambient pressure thermal

20 expansion measurements yielded thermal expansion coefficients $a_0 = 4.9(2) \times 10^{-5}$ and a_1

21 $=3.7(5) \times 10^{-8}$. The combined results allow the derivation of a thermal equation of state.

22 The new data provide constraints on the behavior of carbonates and carbon cycling in the

23 Earth's crust and mantle.

Introduction

24

25   Carbon in the deep Earth consists of a primordial component plus carbonate that

26   has recycled into the Earth's mantle via subduction zones (Dasgupta and Hirschmann

27   2010; Kelemen and Manning, 2015). In the solid state, carbon has limited solubility in

28   mantle silicates and therefore resides chiefly in carbon-rich accessory phases, either as

29   oxidized carbonate or reduced graphite, diamond, or carbide (Shcheka, et al. 2006).

30   Aragonite is one of the two most common forms of calcium carbonate found at the

31   Earth's surface and is formed by both biological and physical processes. Although

32   aragonite is metastable at ambient conditions at the surface of the Earth, its biological

33   formation and contribution to ocean floor deposits and high-pressure stability make it the

34   predominant form of calcium carbonate contributing to deep-Earth recycling at

35   subduction zones. Therefore, understanding the phase stability and compressibility of

36   aragonite at high pressures and temperatures will help constrain the behavior of a key

37   potential carbon reservoir in the deep carbon cycle.

38   At ambient conditions, aragonite has an orthorhombic $2/m\ 2/m\ 2/m$ structure and

39   an average unit cell volume of 226.93(6) $Å^3$ and a Z of 4 (Figure 1) (Martinez et al. 1996;

40   Santillán and Williams 2004; Ono et al. 2005; Antao et al. 2010; Ye et al. 2012).

41   Aragonite becomes stable relative to calcite at ~0.3 GPa (e.g., Johannes and Puhan,

42   1971); however, the pressure of its transformation to a higher pressure (post-aragonite)

43   phase is the subject of debate (Vizgirda and Ahrens, 1982; Kraft et al., 1991; Santillán

44   and Williams, 2004; Ono, 2005; Martinez et al., 1996; Liu et al., 2005). Early shock

45   compression experiments suggested that aragonite undergoes a phase transition around 6

46   GPa with the possibility of another transition at ~16 GPa (Vizgirda and Ahrens, 1982).

47   However, subsequent vibrational spectroscopy experiments found no sign of these phase

48   transitions to 40 GPa (Kraft et al., 1991). X-ray diffraction studies by Santillán and

49   Williams (2004) and Ono et al. (2005) indicated a phase transition near 35-40 GPa but

50   found differing behavior near the transition pressure. Santillán and Williams (2004) noted

51   that strong lattice strain developed between 26 and 40 GPa and suggested that it marked

52   the onset a sluggish transition to a trigonal structure that became complete at 40 GPa. In

53   contrast, Ono et al. (2005) proposed that the transition was a new orthorhombic structure

54   with $Z = 2$. Studies of high pressure $CaCO_3$ by *ab initio* methods focused chiefly on the

55   transition to post-aragonite and pyroxene-type polymorphs (Oganov et al. 2006, 2008;

56   Arapan et al. 2007; Arapan and Ahuja, 2010; Pickard and Needs, 2015) but in some cases

57   results identify additional potentially stable structures in the vicinity of the aragonite to

58   post-aragonite transition (e.g., Pickard and Needs 2015).

59   Insights into the nature and location of the transition to a higher pressure phase

60   can be gained by study of the compressional behavior of aragonite. However, existing X-

61   ray diffraction studies (Martinez et al. 1996; Santillán and Williams 2004; Ono et al.

62   2005) disagree and lack sufficient detail in the pressure range of the transition.

63   To address these issues, we conducted a single-crystal synchrotron X-ray

64   diffraction study of aragonite under hydrostatic compression to 40 GPa at ambient

65   temperature in a diamond anvil cell (DAC). We supplemented compressional results with

66   thermal expansion data from powder X-ray diffraction at ambient pressure. The

67   combination of these studies enables the creation of a complete thermoelastic equation of

68   state for aragonite and provides detailed insights into the polyhedral and atomic

69   distortions that accompany compression in the vicinity of the high pressure breakdown of

70   aragonite.

71   **Methods**

72   The starting sample of aragonite was a natural specimen from Spain (Molina de

73   Aragon) with a pure composition of $CaCO_3$, within experimental accuracy as determined

74   by electron microprobe analysis (University of Milano, Italy). We performed high-

75   pressure single-crystal experiments at the undulator source ID09A beamline at the ESRF,

76   Grenoble, France, following established procedures (Merlini and Hanfland, 2013). The

77   optical features of the beamline provide a near-parallel collimated X-ray beam of

78   approximately 15 x 10 microns^2 on the sample. The sample was loaded in a Ne pressure

79   transmitting medium in a membrane-type diamond anvil cell of Boehler-Almax design

80   equipped with 300 μm culet size diamonds and opening windows of 60 degrees. Pressure

81   was determined using ruby fluorescence (Mao et al., 1986). The DAC was mounted on a

82   Omega-rotation goniometer, and single-crystal data were collected by integrated step-

83   scans of 1 degree, in the 60 degree rotation range allowed by the geometry of the DAC.

84   The diffraction patterns were recorded with the Mar555 flat panel detector, at a distance

85   of 300 mm from the sample. Aragonite was compressed continuously from ambient

86   pressure to 40 GPa in steps of 1-2 GPa to provide good statistics for equation of state

87   fitting (Table 1). The data were processed with the Crysalis software (Oxford Diffraction,

88   2008). The instrumental geometrical parameters (sample to detector distance, beam

89   center and detector tilt) were refined with a garnet standard single crystal. The refinement

90   of crystal orientation matrix provided aragonite lattice parameters at variable pressures.

91   The integrated intensity was used for structure refinement, using the software packages

92   Superflip (Palatinus and Chapuis 2007) and Jana2006 (Petricek et al. 2006).

93   Ambient-pressure thermal expansion measurements were collected on the same

94   natural aragonite sample. Powder diffraction data were collected using a wavelength of

95   0.689264 Å at the MCX beamline at the Elettra synchrotron using previously described

96   techniques (Rebuffi et al. 2014). Powdered aragonite was enclosed in a quartz capillary

97   and mixed with quartz as internal standard. A hot glass blower maintained high

98   temperature and measurements were performed in the temperature interval 298-700 K

99   (Table 2). The temperature precision is estimated using the α-β quartz high

100   temperature transition to be within ± 2°C. The diffraction patterns were analyzed using

101   the Rietveld method and the GSAS software. The extracted unit cell volumes were used

102   to fit a simple linear thermal expansion model (Fei 1995; Angel et al. 2014).

103   **Results**

104   **Phase stability and lattice compressibility**

105   Single-crystal measurements at ambient pressure and temperature confirm the

106   orthorhombic Pnma space group of aragonite and yield a unit cell volume of 226.932(5)

107   $Å^3$. Figure 2 shows the aragonite lattice compression to 36 GPa at ambient temperature.

108   The data indicate a decrease in cell volume of ~25% over this pressure range. Below ~10

109   GPa, our results are in good agreement with powder X-ray diffraction studies that used

110   cubic anvil (Martinez et al., 1996) and diamond-anvil cells (Ono et al., 2005; Santillán

111   and Williams, 2004). At higher pressures, the new data agree well with those of Martinez

112   et al. (1996) and Ono et al. (2005), but differ from the Santillán and Williams (2004)

113   data. The deviation of the volumes determined by Santillán and Williams above 10 GPa

114   likely resulted from freezing of the methanol-ethanol mixture they used as a pressure

115   medium, resulting in non-hydrostaticity in their diamond-cell experiments. Ono et al.

116   (2005) addressed this problem by laser heating their aragonite sample in a DAC to reduce

117   differential pressure effects in the sample chamber and to overcome kinetic inhibition of

118   any phase transitions. Data were collected at ambient temperature after cooling. Their

119   data agree with our results to 27 GPa. The next pressure at which Ono et al. (2005)

120   obtained data was 35 GPa, where they identified a large decrease in volume which they

121   interpret to be due to transformation to post-aragonite structure.

122   The data were fitted to a 3rd order Birch-Murnaghan equation of state using a

123   linear least-squares fitting method with V_0 fixed at 226.932(5) $Å^3$, the ambient pressure

124   measurement. Data at >31.5 GPa begin to depart from the Birch-Murhaghan functional

125   form, perhaps due to lattice distortion signaling the onset of the phase transition. To

126   ensure exclusion of data compromised by lattice distortion, only results from ≤31.5 GPa

127   were used to derive the isothermal equation of state. This yields an isothermal bulk

128   modulus of aragonite of 66.5(7) GPa with K' = 5.0(1). The values agree well with

129   previous values from X-ray diffraction (Martinez et al. 1996; Ono et al. 2005) and

130   Brillouin scattering (Liu et al. 2005) experiments, in which derived bulk moduli were

131   respectively 64.8, 73(2) and 68.9(14) GPa (K' = at 4). Ono et al. also fitted K', obtaining

132   a bulk modulus of 67(6) GPa and K' = 4.7(8), again in excellent agreement with our

133   result.

134   The compressibility of the lattice parameters of aragonite provides insight into the

135   lattice-dependent elasticity, the mechanism of compressibility, and the onset of phase

136   transformations. The pressure evolution of the normalized values of the *a, b*, and *c* lattice

137   parameters of aragonite is shown in Figure 3. The lattice compressibilities were

138   determined by fitting a 3rd order Birch-Murnaghan equation to the cubed lattice

139   parameters as a function of pressure. The *a*-axis is most compressible, with a bulk

140   modulus of 46.0(5) GPa and K'=2.93(5). The *c*-axis is the least compressible with K =

141   122(2) GPa and K'=5.6(3). The *b*-axis displays a change in compressibility at ~15 GPa.

142   Below this pressure, the fit to the data yields a bulk modulus of 59(2) GPa with

143   K'=11.4(7). In contrast, at >15 GPa the pressure dependence flattens, indicating a

144   stiffening of the *b*-axis. Although the relative compressibilities of each lattice parameter

145   follow trends similar to those determined by Santillán and Williams (2004) and Martinez

146   et al. (1996), our values disagree in detail. Martinez et al. (1996) found both the *b* and *c*

147   axes to be more compressible to their highest pressure of 7 GPa. The small pressure range

148   of their experiment limits the accuracy of their results when applied to higher pressure

149   data such as our own. We interpret the difference between our measured compressibilities

150   and the apparent lower compressibility inferred from the Santillián and Williams (2004)

151   data as arising from non-hydrostatic pressure in their sample chamber above 10 GPa.

Axial ratios and polyhedral evolution

153   Figure 4 shows the *c/a*, *b/a* and *b/c* axial ratios as a function of pressure. These

154   plots demonstrate significant mechanical distortion of the aragonite unit cell volume with

155   compression. The *c/a* and *b/a* ratios increase continuously as pressure rises. The *c/a* and

156   *b/c* ratios of Martinez et al. (1996) agree reasonably well with our data to 7 GPa, the

157   highest pressure in their study. Our results also agree with those of Santillán and

158   Williams (2004) below 10 GPa; however, their data become scattered at higher pressures

159   where their cell lost hydrostaticity. The new, more densely spaced measurements reveal

160   that the change in *c/a* ratio on compression is slightly nonlinear (Figure 4a). The

161   curvature indicates that the *a*-axis increases in compressibility relative to the *c*-axis,

162   which is the least compressible axis (Fig. 3). The change in the ratio above 31.5 GPa

163   (dashed black line in Figure 4a) indicates a large increase in the compressibility of the *a*-

164   axis relative to the *c*-axis. The *b/a* ratio is linear throughout its pressure range. A dramatic

165   shift occurs at ~30 GPa where the *b*-axis becomes significantly less compressible than the

166   *a*-axis (Figure 4b). The large change in slope arises from commensurate increase in *a*-

167   axis compressibility and decrease in *b*-axis compressibility above 30 GPa.

168   The *b/c* ratio (Figure 4c) decreases to a minimum at ~15 GPa and then increases

169   slightly to ~30 GPa. The *b/c* ratio rises dramatically above this pressure. This behavior is

170   confirmed (as well as the patterns in 4a and 4b) by an additional dataset taken at high

171   pressure and included in this study as Supplemental Material. Data from Martinez et al

172   (1996) and Santillán and Williams (2004) show a similar trend to ~10 GPa, as with *c/a*

173   and *b/a*, the data of Santillán and Williams (2004) deviate at higher pressure. As with the

174   *b/a* ratio, the change in slope in *b/c* at ~30 GPa is an indication of severe stiffening of the

175   *b*-axis (Fig. 3). Santillán and Williams (2004) noted that when the *b/c* ratio reaches 1.73

176   = the orthorhombic symmetry degenerates to trigonal symmetry. Santillán and Williams

177   (2004) found this to occur at 40 GPa and our data support evolution toward this value due

178   to the stiffening of the *b*-axis. Subsequent work by Ono et al. (2005) and (2007) indicate

179   that the post-aragonite phase is orthorhombic and that the transition pressure is lower

180   than that expected for the breakdown to trigonal symmetry. We are likely seeing evidence

181   for structural distortions at or near conditions of aragonite breakdown as the axial ratios

182   diverge abruptly from their previous trends.

183   The compressibility of the axes is directly related to the orientation and

184   compressibility of the constituent polyhedra. The plane created by the *b* and *c* axes is

185   parallel to the carbonate groups in the aragonite structure, whereas the *a*-axis is

186   perpendicular to them (Figure 5). The high compressibility of the *a*-axis results from the

187   orientation the relatively rigid carbonate groups, which give no support to compression

188   along the *a*-axis (Ross and Reader 1992). Accordingly, compression is accommodated by

189   geometric changes in the Ca-O polyhedra. The average compression of the Ca-O

190   polyhedra below 31.5 GPa, as fit to the 3rd order Birch-Murnaghan equation of state,

191   gives a bulk modulus of 62(2) GPa with K'=7.1(5). This is within error of the

192   compressibility of the *b*-axis below 15 GPa and is likely the initial driving force of its

193   compression.

194   Unlike the Ca-O polyhedra, the carbonate groups are relatively incompressible at

195   these pressures (though they do exhibit small but significant distortions; see below). At

196   ambient pressure and temperature, the distance between triangular carbonate groups is

197   2.881(13) Å along the *a*-axis, 4.949(5) Å along the *c*-axis and 7.942(15) Å along the *b*-

198   axis. The change in these separations with pressure is a good indicator of the

199   compressiblities of the axes with which they are aligned. Figure 5 compares the aragonite

200   unit cell at ambient pressure and at 31.5 GPa. The carbon and O2 atoms lie along the *b*-

201   axis and the base of the carbonate triangle lies along the *c*-axis. A decrease in the end-to-

202   end separation of the relatively rigid carbonate triangles and the alignment of the triangle

203   base with the *c*-axis account for its lower compressibility. The increasing compressibility

204   of the *a*-axis is due in part to the small tilting of the carbonate groups, identifiable by the

205   O2 atoms dipping out of the *b-c* plane toward the *a*-axis.

206   Figure 6 compares the ratio of the distances between the carbonate groups along

207   the *c* and *b* axes to the *b/c* ratio (Figure 4c). The nearly identical dependence on pressure

208   suggests that the intercarbonate distances control the changes in *b/c* axial ratio. Study of

209   the carbonate-carbonate distances identifies two dips in *b/c* at ≥30 GPa. These dips may

210   be caused by the effects of the distortion of the carbonate groups on the lattice parameters

211   and intracellular dynamics (discussed further in the next section). Measurements of the

212   carbonate separation distance indicate that the *b*-axis becomes less compressible starting

213   at ~15 GPa and that it becomes stiffer than the *c*-axis between 25-30 GPa. This is

214   consistent with an upcoming phase transition between 30 and 40 GPa, as found

215   experimentally by Santillán and Williams (2004) and Ono et al. (2005), and predicted by

216   ab initio studies (Oganov et al. 2006; Arapan and Ahuja 2010; Pickard and Needs 2015).

217   The post-aragonite structure found by Ono et al. (2005) has a lower Z (2, not 4) and its *b*-

218   axis is ~40% shorter with respect to the *a* and *c*-axes than that found in the ambient

219   orthorhombic aragonite structure. This reduction in the relative *b*-axis length is smaller

220   than the 50% decrease in formula unit (Z) and indicates that the b-axis remains stiff in the

221   new structure. Experimental work on the lattice geometry of post-aragonite is needed to

222   confirm this conclusion.

223   **Atomic evolution and polyhedral distortion**

224   The evolution with pressure of the atomic positions in the unit cell is shown in

225   Figure 7. The carbon atoms at the center of the carbonate groups move with the O1

226   atomic position in both *a* and *c* axial directions. With compression, the carbon and O1

227   positions show little movement and no correlation along the *b*-axis, which is consistent

228   with their nearly perpendicular alignment in this direction (Figure 5). The Ca atomic

229   position moves linearly in each axial direction and undergoes only a minor shift in

230   position, consistent with the oxygen atoms compressing around a relatively stationary Ca

231   atom. The O2 atomic position remains fairly constant in its position along the *c*-axis, but

232   undergoes notable changes in the other two atomic planes. This observation is consistent

233   with large compressional displacement along the *a*-axis as the stacked carbonate groups

234   move closer together and tilt and with the changing compressibility of the *c*-axis. Along

235   the *a*-axis, the O2 position increases with respect to its original position to ~25 GPa, and

236   then dips back toward its original coordinate at 25-30 GPa, the same pressure range as the

237   dip in CO_3-CO_3 distance along the *b*-axis (Fig. 6). Similar behavior is seen in the *b*-axis

238   where the O2 position initially has a negative linear trend compared to its initial position

239   that becomes a reversal near 25 GPa, much like the behavior seen in the *b/c* axial ratio in

240   Figure 4c and the evolution of the carbonate spacing ratio in Figure 6. These shifts bring

241   the O2 position out of initial alignment with both carbon and calcium atoms as can be

242   seen in the *b-c* plane slices at 0 and 31.5 GPa in Figure 5. Figure 5 shows that the central

243   carbon atom in both carbonate groups displaces to left during pressure increase, creating

244   a distortion of the CO_3 triangles in the *b-c* plane. In addition, the O2 atoms dip into *a*-

245   axis as the carbonate planar groups tilt slightly into the *b-c* plane with the O2 arrow side

246   tilting down.

247   The carbonate groups undergo small but important changes in geometry. Figure 8

248   gives the evolution of the bonds (Fig. 8a) and angles (Fig. 8b) within the carbonate

249   structure. Both the C-O1 and C-O2 bond lengths remain within close range of their

250   ambient values ≤20 GPa. Above this pressure the bond lengths between the C-O1 and C-

251   O2 diverge. The C-O2 bond continuously shortens between 20 GPa and 31.5 GPa where

252   C-O bong length measurements became unreliable due to lattice distortion. The C-O1

253   bond length increases over the same pressure range, although at a less dramatic rate. The

254 bond angles reflect the changing geometry demonstrated in the bond lengths. At ambient

255 pressure, the carbonate groups define equilateral triangles, with both bond angles equal to

256 120°. Distortion begins almost immediately and the bond angles do not return to 120° as

257 compression continues. The O1-C-O1 bond angle decreases while the two O1-C-O2 bond

258 angles increase before relaxing slightly near ~20 GPa. This divergence occurs before any

259 noticeable changes in bond length arise in the same pressure range (Figure 8a). Above

260 ~20 GPa the two O1-C-O2 bond angles continually diverge from the O1-C-O1 angle and

261 the two types end with a 20° difference in angle at 31.5 GPa. The 106° O1-C-O1 angle is

262 even smaller than the tetrahedral bonding angle of 109.5° found in four-coordinated

263 structures.

264   These changes in the carbonate groups are visualized in the overlaid carbonate

265 triangles in Figure 9. The groups clearly evolve from an equilateral to an isosceles

266 triangle at high pressure. The tilt of the O2 atoms in the *a*-axis is apparent in Figure 9b

267 and 9c, which also shows a small deflection of the O1-C-O1 stacking from linear. The

268 stages of change in the carbonate groups are in alignment with the changes observed in

269 the *b/c* ratio. The decrease in bond length and divergence in angle are concurrent with the

270 reversal in the *b*/c ratios in Figures 4c and 6. The increase in slope and significant

271 reduction in the compressibility of the *b*-axis correlate directly with the divergence in

272 both bond length and angle and the shift from equilateral to isosceles. Compression along

273 the *b*-axis begins to stiffen as soon as the carbonate groups begin to distort effecting the

274 overall lattice and leading the rebound in the *b/c* ratio. Effects on other lattice parameters

275 are not apparent until near ~30 GPa when all the ratios under and abrupt change in slope

276 (Figure 4).

277   The distance from the O2 atoms to the base of the triangular carbonate group

278   decreases by 1.9% to 31.5 GPa while the *b*-axis itself compresses 6.2%. This difference is

279   another illustration of how the distortion of the carbonate group contributes to increasing

280   stiffness along the *b*-axis with pressure. The *c*-axis compresses evenly despite the bond

281   angle between O1-C-O1 decreasing by 16° over the entire pressure range. The carbonate

282   group O1-O1 distance decreases by 5.6% to 31.5 GPa, essentially the same as the *c*-axis

283   at 5.2% compression over the same range. Thus, the compressional behavior of aragonite

284   can be seen to be a consequence of small, but significant, changes in the most rigid

285   polyhedral elements, the carbonate groups.

286   **Thermal expansion**

287   Figure 10 shows the ambient pressure thermal expansion data gathered during the

288   powder X-ray diffraction experiment. The measurements are in good agreement with

289   previous data from both Antao et al. (2010) and Ye et al. (2012). The thermal expansion

290   of aragonite was fitted using the formalism:

291     $V(T) = V_0 Exp\left\{\int_{T_{Ref}}^{T} a_V(T)\, dT\right\}$ (1)

292     $\alpha_V(T) = a_0 + a_1(T)$ (2)

293   Where $\alpha_v(T)$ is thermal expansion, a_0 and a_1 are fitted constants, V_0 is the ambient

294   temperature volume, T is the temperature and T_{ref} is a reference temperature, usually 300

295   K. The fit of the new thermal expansion data provide the following coefficients: $a_0 =$

296     $4.9(2) \times 10^{-5}$ and $a_1 = 3.7(5) \times 10^{-8}$. These results are in agreement with recent

297   measurements by Ye et al. 2012 yielding $a_0 = 4.6(2) \times 10^{-5}$ and $a_1 = 5.4(4) \times 10^{-8}$ (143-

298   586 K), but conflict with other literature data (Antao et al. 2010; Martinez et al. 1996).

299   Antao et al. (2010) found $a_0 = 5.47(4) \times 10^{-5}$ and $a_1 = 6.1(2) \times 10^{-8}$ (300-750 K), which is

300   11% greater in a_0 and 64% larger in a_1. Figure 10 indicates that the data from Antao et al.

301   (2010) are in exceptional agreement with the new measurements, which implies that the

302   discrepancy must be in the fitting process. All the experiments indicate that the *a*-axis

303   exhibits the greatest thermal expansion, and the *c*-axis the least. The thermal results

304   correlate well with the compressibility study. The *a*-axis is the most compressible and the

305   most expandable. The *c*-axis is the least compressible and the least expandable.

306   **Implications**

307   This study has generated a new isothermal equation of state for aragonite up to 40

308   GPa, where aragonite likely undergoes a phase transformation. Our new equation of state

309   agrees with previous hydrostatic data (Ono et al., 2005; Liu et al., 2005) and our

310   observation of structural changes at high pressures agrees with previous observations

311   (Martinez et al., 1996; Santillán and Williams, 2004; Ono et al., 2005), but the equation

312   benefits from higher sampling density and improved precision in the present study. Our

313   measurements also permit quantification of the evolution with pressure of the aragonite

314   axial parameters and the internal behavior of the polyhedral constituents of the unit cell.

315   Significantly, we have identified a reduction in the compressibility of the *b*-axis, which is

316   directly linked to distortions of the carbonate groups and their change from equilateral to

317   isosceles. The distortion of the carbonate groups through the divergence of the C-O1 and

318   C-O2 bond lengths is especially intriguing. Future study of such internal displacements in

319   the carbonate group may give insight into its transformation into a 4-coordinated

320   tetrahedral as predicted by Oganov et al. (2006), Arapan et al. (2007) and Arapan and

321   Ahuja (2010) and experimentally observed in aragonite by Ono et al. (2007), in Fe-rich

322   carbonates by Boulard et al. (2012), in ferromagnesite by Boulard et al. (2015) and in

323    $Mg_2Fe_2C_4O_{13}$ by Merlini et al. (2015).

324   These results also provide insight into the distortion of the aragonite structure

325   before the phase transition, which is both predicted (Oganov et al. 2006; Arapan and

326   Ahuja 2010; Pickard and Needs 2015) and observed between 30-40 GPa (Santillán and

327   Williams 2004; Ono et al. 2005). Using *ab initio* calculations Pickard and Needs (2015)

328   predict a monoclinic $P2_1/c$ structure to be most stable between 32-48 GPa, which

329   correlates directly with our abrupt change in axial ratios and the appearance of large

330   lattice distortion above 31.5 GPa. Our data validate a transition in the range, but give no

331   further insight in the exact structure adopted by Aragonite at these pressures. Indeed, this

332   new structure does not exactly fit previous experimental data of post aragonite found by

333   Ono et al. (2005), but there may be kinetic effects hindering the transition or

334   discrepancies caused by the laser heating techniques used in the experimental study.

335   Nevertheless, the aragonite data in this study provides significant insight into the

336   behavior of aragonite and its constituent polyhedra as these transition pressures approach.

337   Kinetic effects may explain why our data maintain the distorted aragonite structure to the

338   highest pressure we could extract good data from, 34.8 GPa, instead of undergoing a

339   transition. The diverging axial ratios and distortion of the lattice indicate that a transition

340   may be taking place sooner than the 40 GPa pressure reported in previous studies.

341   Our thermal expansion data bolsters the database of aragonite's thermal expansion

342   measurements and confirms the findings of previous studies (Ye et al. 2012). The

343   combination of the new thermal expansion data with the equation of state generated in

344   this work will provide an accurate thermoelastic equation of state. This thermal equation

345   of state can be used to model planetary interiors and provide further insight into carbon

346   storage within the deep earth.

347

348   **Acknowledgements**

349   Thanks to the Deep Carbon Observatory for providing travel assistance for S. Palaich.

350   This work was funded in part by NSF EAR-0969033 and DOE NNSA Stewardship

351   Science Graduate Fellowship to S. Palaich, DOE DE-FG02-10ER16136. ESRF and

352   Elettra facilities are acknowledged for provision of beamtime. Paolo Lotti is

353   acknowledged for help in the experimental activity.

354

References

Angel, R.J., Gonzalez-Platas, J., and Alvaro, M. (2014) EosFit7c and a Fortran module (library) for equation of state calculations. Zeitschrift fur Kristallographie, 30, 405-419.

Antao, S.M. and Hassan, I. (2010) Temperature dependence of the structural parameters in the transformation of aragonite to calcite, as determined from *in situ* synchrotron powder X-ray-diffraction data. The Canadian Mineralogist, 48, 1225-1236.

Arapan, S., and Ahuja, R. (2010) High-pressure phase transformations in carbonates. Physical Review B, 82, no. 18, 184115.

Arapan, S., Souza de Almeida, J., and Ahuja, R. (2007) Formation of sp^3 Hybridized Bonds and Stability of $CaCO_3$ at Very High Pressure. Physical Review Letters, 98, 268501.

Boulard, E., Menguy, N., Auzende, A.L., Benzerara, K., Bureau, H., Antonangeli, D., Corgne, A., Morard, G., Siebert, J., Perrillat, J.P., Guyot, F., and Fiquet, G. (2012) Experimental investigation of the stability of Fe-rich carbonates in the lower mantle. Journal of Geophysical Research, 117, B02208.

Boulard, E., Pan, D., Galli, G., Liu, Z., and Mao, W.L. (2015) Tetrahedrally coordinated carbonates in Earth's lower mantle. Nature Communications, 6, 6311.

Dasgupta, R., and Hirschmann, M.M. (2010) The deep carbon cycle and melting in Earth's interior. Earth and Planetary Science Letters, 298, 1–13.

Fei, Y. (1995) Thermal Expansion. In T.J. Ahrens, Ed., Mineral physics and crystallography: a handbook of physical constants, p. 29-45. American Geophysical Union, Washington, D.C.

Kelemen, P.B., Manning, C.E. (2015) Reevaluating carbon fluxes in subduction zones, what goes down, mostly comes up. Proceedings of the National Academy of Sciences, 112, E3997-E4006.

Kraft, S., Knittle, E., and Williams, Q. (1991) Carbonate stability in the Earth's mantle: A vibrational spectroscopic study of aragonite and dolomite at high pressures and temperatures. Journal of Geophysical Research, 96, 17–997–18–009.

Liu, L.-G., Chen, C.-C., Lin, C.-C., and Yang, Y.-J. (2005) Elasticity of single-crystal aragonite by Brillouin spectroscopy. Physics and Chemistry of Minerals, 32, 97–102.

Mao, H.-K.K., Xu, J.-A., and Bell, P.M. (1986) Calibration of the Ruby Pressure Gauge to 800 kbar. Journal of Geophysical Research, 91, 4673–4676.

Martinez, I., Zhang, J., and Reeder, R.J. (1996) In situ X-ray diffraction of aragonite and

391   dolomite at high pressure and high temperature; evidence for dolomite breakdown to
392   aragonite and magnesite. American Mineralogist, 81, 611–624.

393 Merlini, M. and Hanfland, M. (2013) Single-crystal diffraction at megabar conditions by
394   synchrotron radiation. High Pressure Research, 33, 511-522.

395 Merlini, M., Hanfland, M., Salamat, A., Petitgirard, S., and Mueller H. (2015) The
396   Crystal Structures of $Mg_2Fe_2C_4O_{13}$, with tetrahedrally coordinated carbon, and
397    $Fe_{13}O_{19}$, synthesized at deep mantle conditions. American Mineralogist, in press.
398   Doi:10.2138/am-2015-5369.

399 Oganov, A.R., Glass, C.W., and Ono, S. (2006) High-pressure phases of CaCO3: Crystal
400   structure prediction and experiment. Earth and Planetary Science Letters, 241, 95–
401   103.

402 Oganov, A.R., Ono, S., Ma, Y., Glass, C.W., and Garcia, A. (2008) Novel high-pressure
403   structures of MgCO3, CaCO3 and CO2 and their role in Earth's lower mantle. Earth
404   and Planetary Science Letters, 273, 38–47.

405 Ono, S., Kikegawa, T., Ohishi, Y., and Tsuchiya, J. (2005) Post-aragonite phase
406   transformation in CaCO3 at 40 GPa. American Mineralogist, 90, 667–671.

407 Ono, S., Kikegawa, T., and Ohishi, Y. (2007) High-pressure transition of CaCO3.
408   American Mineralogist, 92, 1246–1249.

409 Oxford Diffraction (2006) *CrysAlis*. Oxford Diffraction Ltd, Abingdon, England.

410 Palatinus, L. and Chapuis, G. (2007) SUPERFLIP - a computer program for the solution
411   of crystal structures by charge flipping in arbitrary directions. Journal of Applied
412   Crystallography, 40, 786-790.

413 Petricek, V., Dusek, M., and Palatinus, L. (2006). Jana2006: The crystallographic
414   computing system. Institute of Physics, Praha, Czech Republic, http://jana.fzu.cz/.

415 Pickard, C. J., and Needs, R. J. (2015). Structures and stability of calcium and
416   magnesium carbonates at mantle pressures. Physical Review B, 91, 104101.
417
418 Rebuffi, L., Plaisier, J.R., Abdellatief, M., Lausi, A., and Scardi, P. (2014) MCX: a
419   Synchrotron Radiation Beamline for X-ray Diffraction Line Profile Analysis.
420   Zeitschrift fur anorganische und allgemeine Chemie, 640, 3100-3106.
421
422 Ross, N.L. and Reader, R.J. (1992) High-pressure structural study of dolomite and
423   ankerite. American Mineralogist, 77, 412-421.
424
425 Santillán, J., and Williams, Q. (2004) A high pressure X-ray diffraction study of
426   aragonite and the post-aragonite phase transition in CaCO3. American Mineralogist,
427   89, 1348–1352.

428   Shcheka, S.S., Wiedenbeck, M., Frost, D.J., and Keppler, H. (2006) Carbon solubility in
429   mantle minerals. Earth and Planetary Science Letters, 245, 730–742.

430   Vizgirda, J., and Ahrens, T.J. (1982) Shock compression of aragonite and implications
431   for the equation of state of carbonates. Journal of Geophysical Research: Solid Earth,
432   87, 4747–4758.

433   Ye, Y., Smyth, J.R., and Boni, P. (2012) Crystal structure and thermal expansion of
434   aragonite-group carbonates by single-crystal X-ray diffraction. American
435   Mineralogist, 97, 707–712.

436
437

438   **Figure Captions**

439   Figure 1. Structure of aragonite at ambient pressure and temperature. A. View along the

440   *b*-axis; B. View along the *c*-axis; C. Slice through the *a, b* and *c* planes. Aragonite is

441   comprised of two planes of triangular carbonate groups in opposite orientation with 9-

442   coordinated Ca ions between the carbonate groups. Oxygen atoms are red, Ca atoms and

443   polyhedra are blue and C atoms and triangles are grey. The oxygen atoms in the O2

444   position are marked accordingly in each orientation.

445   Figure 2. Aragonite unit cell volume versus pressure. Volume versus pressure data from

446   this study and three previous investigations of aragonite. The dashed black line represents

447   the fit of the data to the 3rd order Birch-Murnaghan equation of state. The starred point in

448   Ono et al.'s (2005) data is a post-aragonite structure found after heating by the authors at

449   35 GPa.

450   Figure 3. Compressiblity of *a, b*, and *c* crystallographic axes of aragonite. The *a*-axis is

451   the most compressible and the *c*-axis is the least compressible. The *b*-axis changes its

452   compression behavior and begin to stiffen ~20 GPa. The data from Santillán and

453   Williams (2004) is consistent to 10 GPa, which is the pressure at which their

454   methanol:ethanol pressure medium freezes and becomes non-hydrostatic.

455   Figure 4.*c/b* (a), *b/a* (b) and b*/c* (c) ratios of aragonite. Data from two previous studies are

456   included in all three figures. The *c/b* ratio in (a) maintains a constant trend (red line) until

457   30 GPa and then changes to steeper slope (dashed line). The *b/a* ratio is linear

458   throughout. The ratio with constant slope to ~30 GPa (red line) before dramatically

459   shifting to a steeper grade (dashed line). The *b/c* ratios declines steadily to 15 GPa and

460   begins to bottom out, remaining nearly constant to 30 GPa (red line) where it shoots up in

461   a linear trend (dashed line). Each of these changes are consistent with the stiffening of the

462   b-axis relative to the a and c axes.

463   Figure 5. Unit cell comparison at ambient and 31.5 GPa. Shows slice through the a-axis,

464   with the c-axis in the vertical and b-axis in the horizontal. Oxygen atoms are red, carbon

465   are black and Ca are light blue. The carbonate groups are white. The ambient pressure

466   unit cell is overlaid (dashed rectangle) over the unit cell at 31.5 GPa to emphasize the

467   changes in both the b and c axes.

468   Figure 6. b/c ratio from unit cell parameters and CO_3-CO_3 distances. The solid black

469   squares are the same as those found in Figure 4c. The open blue squares give the ratio of

470   the distance between carbonate groups along the b-axis and carbonate groups along the c-

471   axis (best visualized in Figure 5). The ratio of the inter-carbonate distances is nearly

472   identical to that of the unit cell parameters and follows the decreasing trend followed by a

473   change in slope at 30 GPa, which is consistent with the distance between carbonate

474   groups along the b-axis ceasing to decrease after ~20 GPa due to the elongation of the

475   carbonate triangles along the b-axis.

476   Figure 7. Pressure-dependent atomic positions. From the single crystal refinement data

477   the evolution of the atomic sites is plotted as a function of pressure in the a, b and c

478   orientations. Positions are plotted as distance from original position in Angstroms,

479   normalized for contracting unit cell volume.

480   Figure 8. C-O bond lengths (a) and O-C-O bond angles (b). The carbon and oxygen bond

481   lengths are shown for both the O1 and O2 sites. The O1 sites are parallel to the c-axis,

482   comprise the base of the carbonate triangle and change very little with pressure. The O2

483   site bisects the base of the triangle and is in alignment with the *b*-axis. At ~20 GPa the C-

484   O2 bond distance rapidly decreases and in turn leads to the U-shaped behavior in the *b/c*

485   ratio and eventual lattice distortion between 25-30 GPa. The bond angles steadily diverge

486   from ~ 20 GPa onward, in alignment with the U-shape in Figure 4c and 6.

487   Figure 9. Evolution of the carbonate groups in the aragonite structure overlaid at two

488   pressures from three angles: *b-c* planar view with significant changes in bond lengths and

489   angles labeled (a), *a-c* planar view where the displacement of the O2 oxygen is noticeable

490   (b) and *a-b* planar illustrating the change in angle between O1-C-O2. The carbonate

491   groups with all atoms gray are extracted from data at 0 GPa. Carbonate groups with

492   oxygen atoms in red are extracted from data at 31.5 GPa. Carbonate is shown in gray in

493   the center and oxygen is either gray or red depending on pressure. O1 and O2 oxygen

494   sites are labeled.

495   Figure 10. Thermal expansion of aragonite unit cell volume and axial crystallographic

496   parameters. Thermal expansion data from our study is shown in solid black. Data from

497   Ye et al. (2012) and Antao et al. (2010) is provided for comparison. We find the *c*-axis to

498   exhibit the most expansion and the *a*-axis to be the least expansive. This is in direct

499   contrast to the compressional behavior where *a* is the most compressible and *c* is the

500   least.

501

502   Table 1.

Pressure	a	b	c	Volume
0	5.741(4)	7.97(1)	4.959(5)	226.9(2)
0.570(1)	5.712(4)	7.942(2)	4.9491(8)	224.5(2)
1.2(1)	5.690(4)	7.922(2)	4.9433(6)	222.8(2)
2.28(9)	5.651(4)	7.886(2)	4.9276(7)	219.6(2)
2.96(7)	5.627(4)	7.865(2)	4.9192(7)	217.7(2)
3.8(2)	5.602(4)	7.846(3)	4.913(6)	215.9(2)
6.0(1)	5.533(4)	7.789(3)	4.8866(6)	210.6(2)
8.0(2)	5.474(4)	7.743(3)	4.8655(4)	206.2(2)
9.9(2)	5.429(4)	7.711(3)	4.8511(6)	203.1(2)
11.6(2)	5.383(4)	7.675(3)	4.8327(7)	199.6(2)
13.8(3)	5.339(4)	7.651(3)	4.8190(8)	196.9(2)
15.7(6)	5.287(4)	7.616(3)	4.7997(7)	193.2(2)
17.5(5)	5.257(4)	7.598(3)	4.7874(8)	191.2(2)
19.5(3)	5.216(4)	7.580(3)	4.7749(8)	188.8(2)
21.1(4)	5.184(4)	7.558(3)	4.7583(8)	186.4(2)
22.8(2)	5.153(4)	7.542(3)	4.7487(8)	184.5(2)
24.03(2)	5.130(4)	7.538(3)	4.7408(8)	183.3(2)
25.38(7)	5.117(4)	7.527(3)	4.7367(8)	182.4(2)
26.7(1)	5.09(4)	7.514(3)	4.7270(8)	180.9(2)
27.9(1)	5.076(4)	7.504(3)	4.7168(8)	179.6(2)
29.1(2)	5.058(4)	7.490(3)	4.7130(8)	178.5(2)
31.4(2)	5.026(4)	7.475(4)	4.6980(8)	176.5(2)
32.9(2)	4.986(2)	7.502(4)	4.687(4)	175.3(2)
34.8(3)	4.948(2)	7.507(4)	4.663(4)	173.2(2)

503

504   Table 2

T (K)	a	b	c	Volume
298	5.7457(2)	4.9638(2)	7.9728(3)	227.39(2)
303	5.7462(2)	4.9634(2)	7.9722(3)	227.37(2)
323	5.7501(2)	4.9644(2)	7.9748(3)	227.65(2)
348	5.7553(2)	4.9655(2)	7.9789(3)	228.02(2)
373	5.7603(2)	4.9671(2)	7.982(3)	228.38(2)
398	5.7661(2)	4.9676(2)	7.9858(3)	228.75(2)
423	5.7716(2)	4.9687(2)	7.9899(3)	229.13(2)
473	5.7822(2)	4.9711(2)	7.9961(3)	229.84(2)
523	5.7931(2)	4.9734(2)	8.0054(3)	230.65(2)
573	5.8035(2)	4.9754(2)	8.0151(3)	231.44(2)
623	5.8149(2)	4.978(2)	8.024(3)	232.27(2)
673	5.8279(2)	4.9794(2)	8.033(3)	233.11(2)

505
506
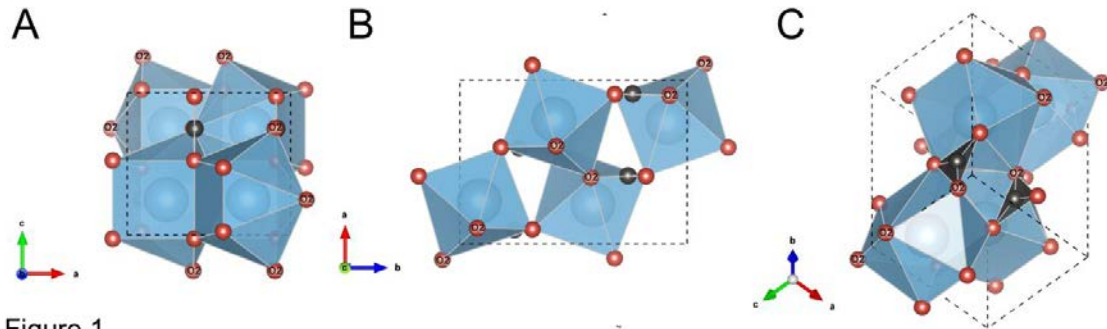
Figure 1
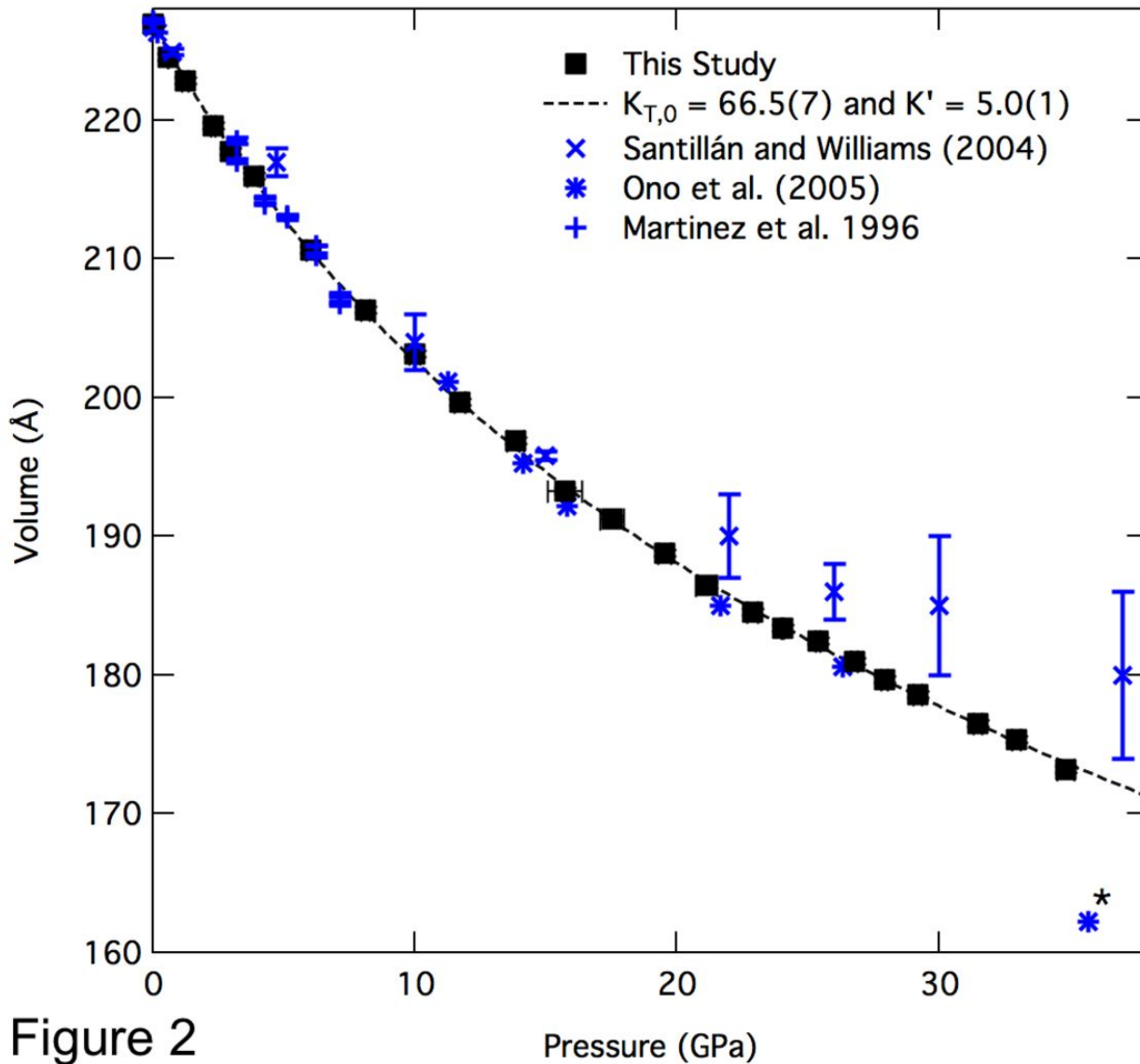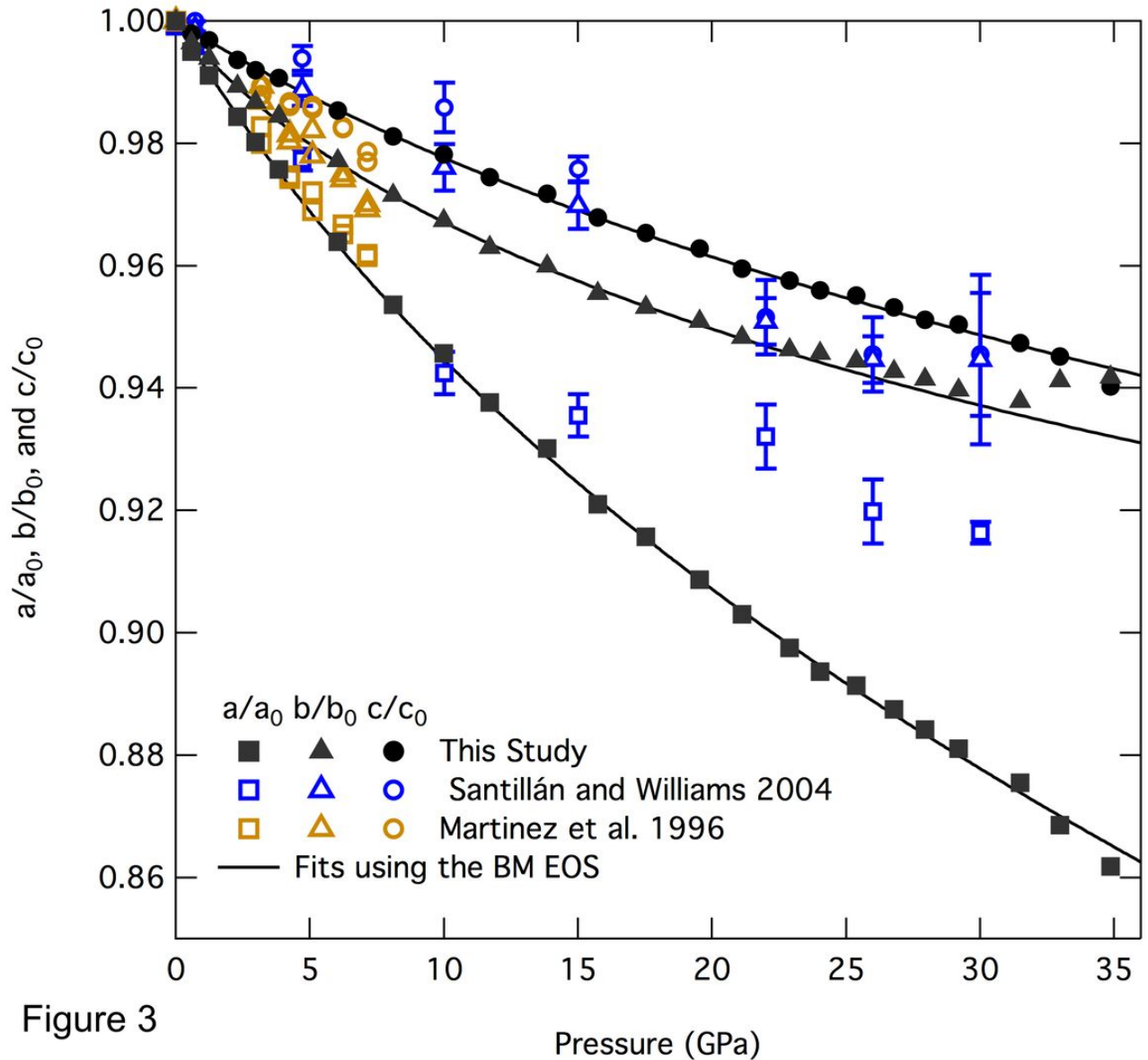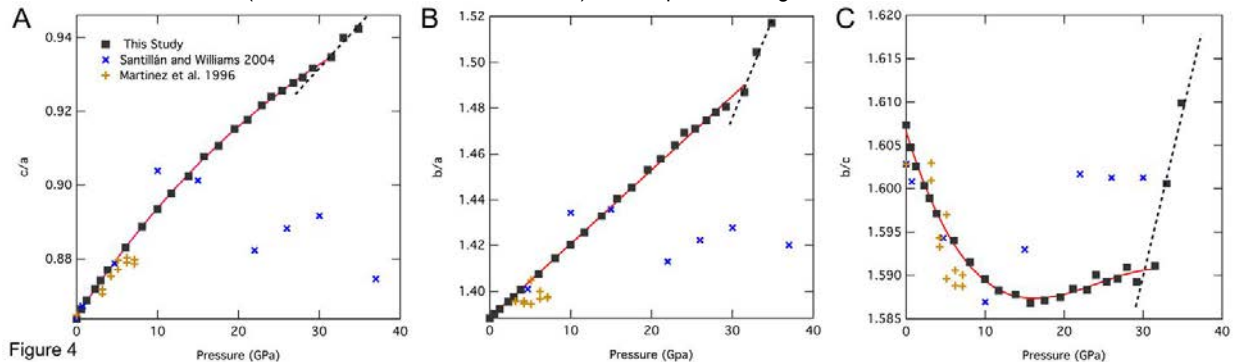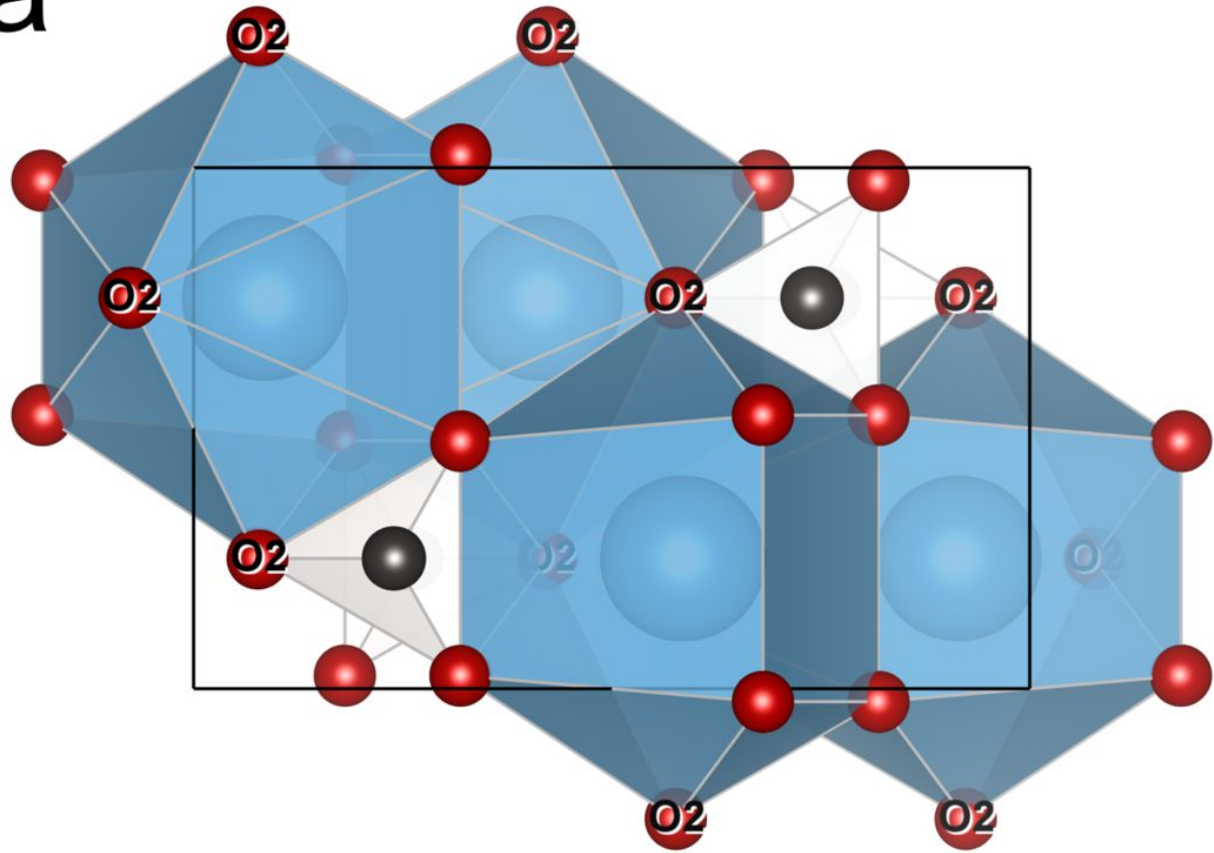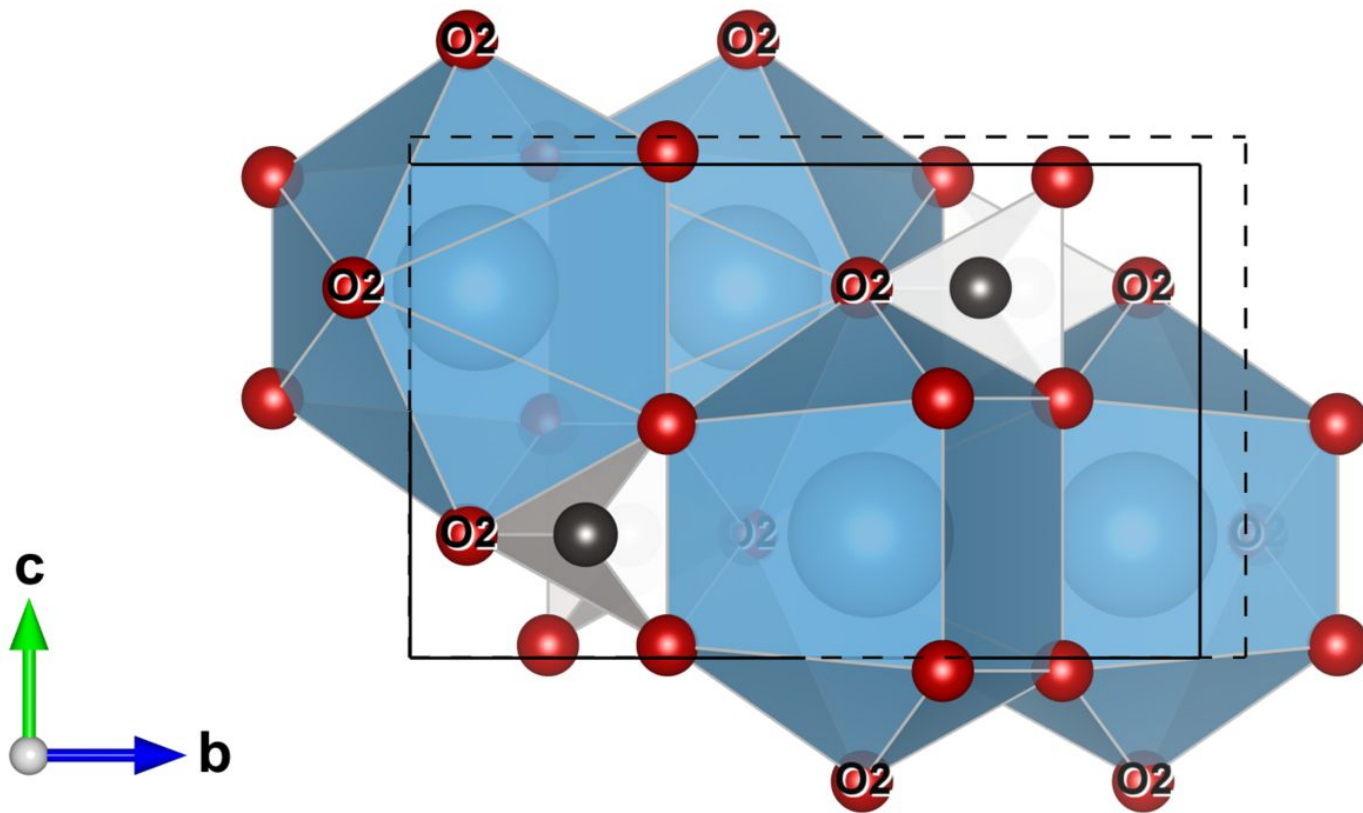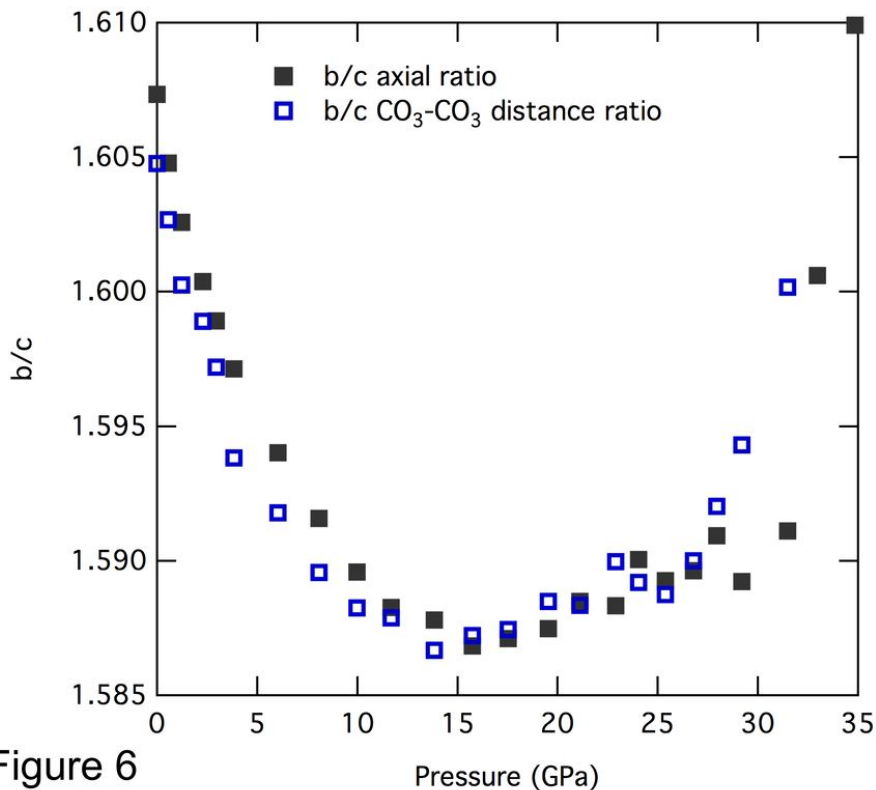
Figure 2

Figure 3
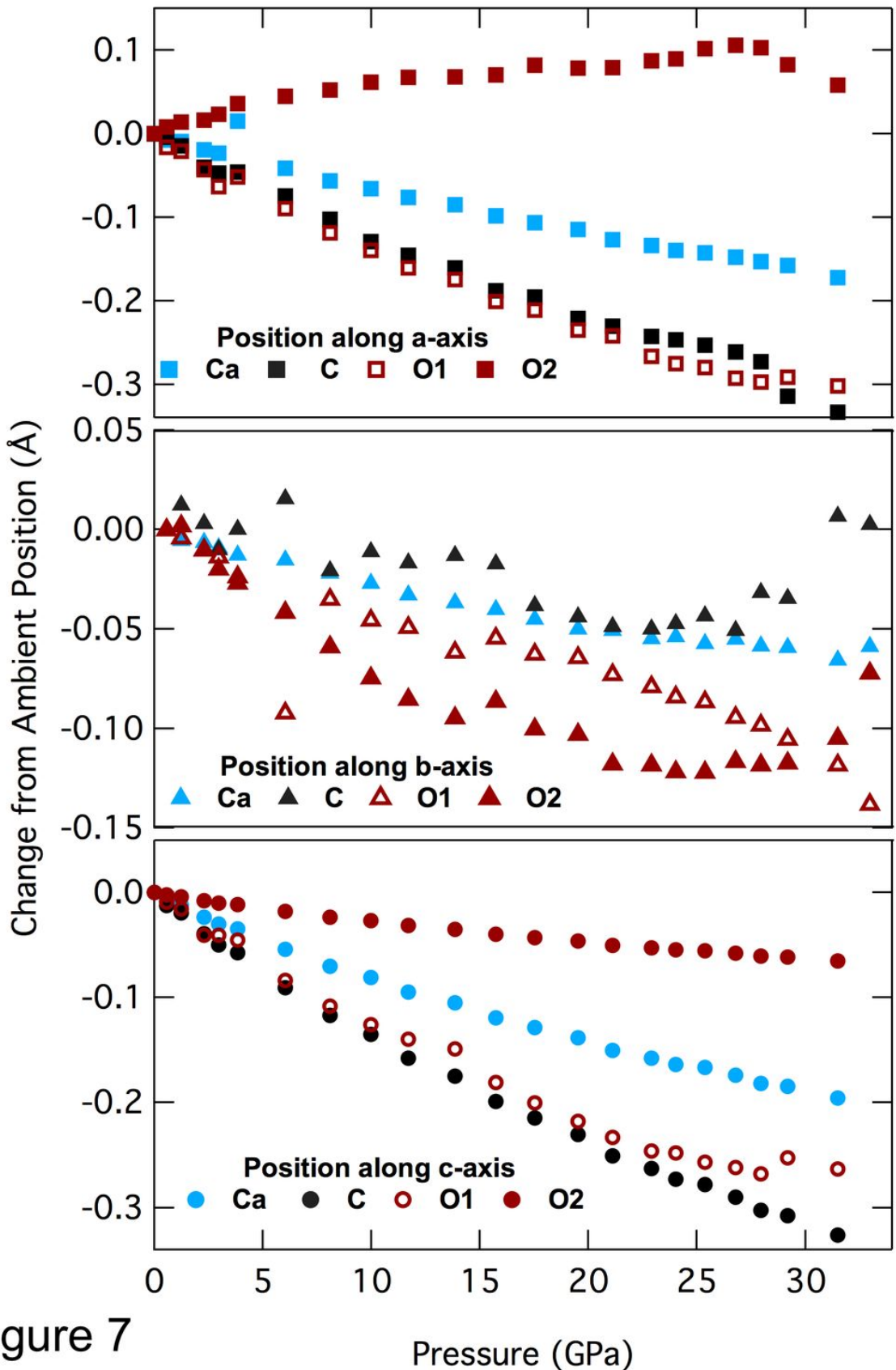
Figure 4

Figure 5
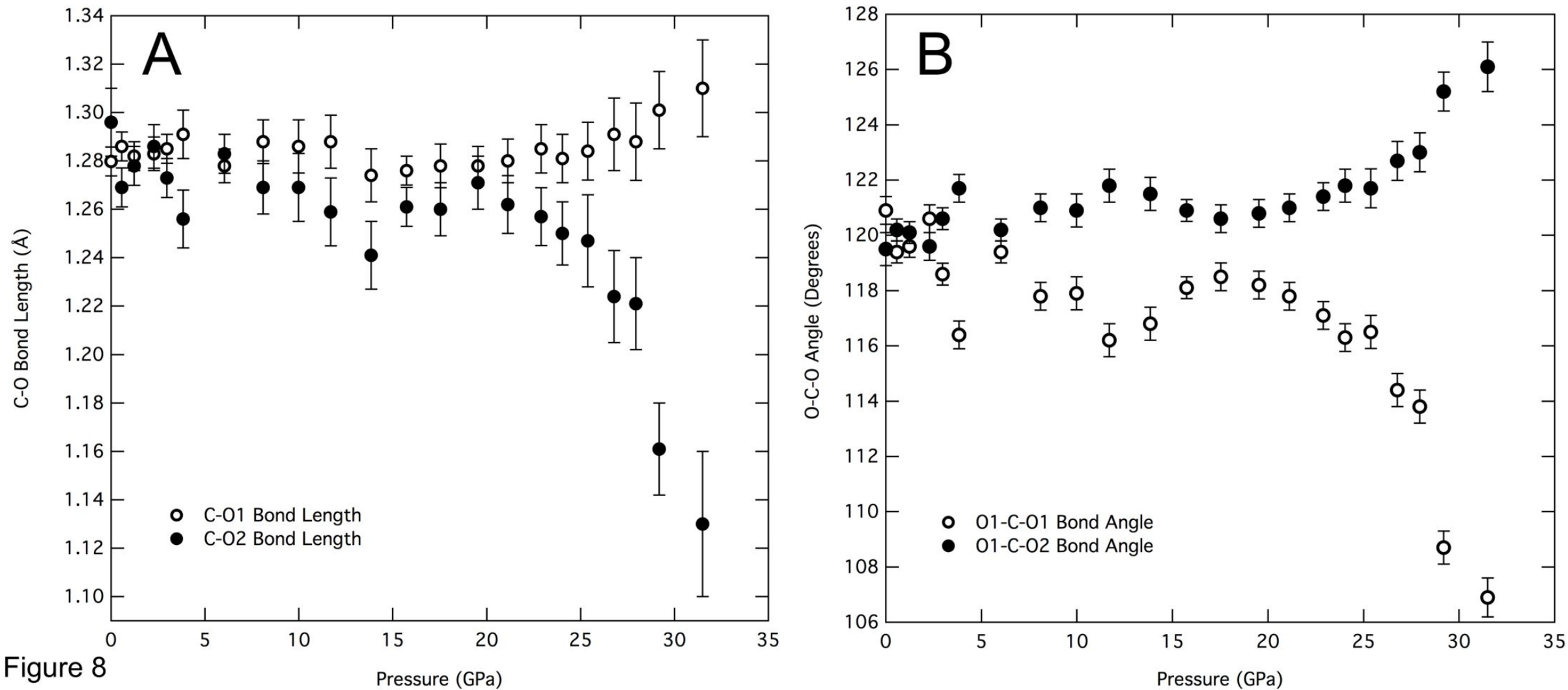
Figure 6
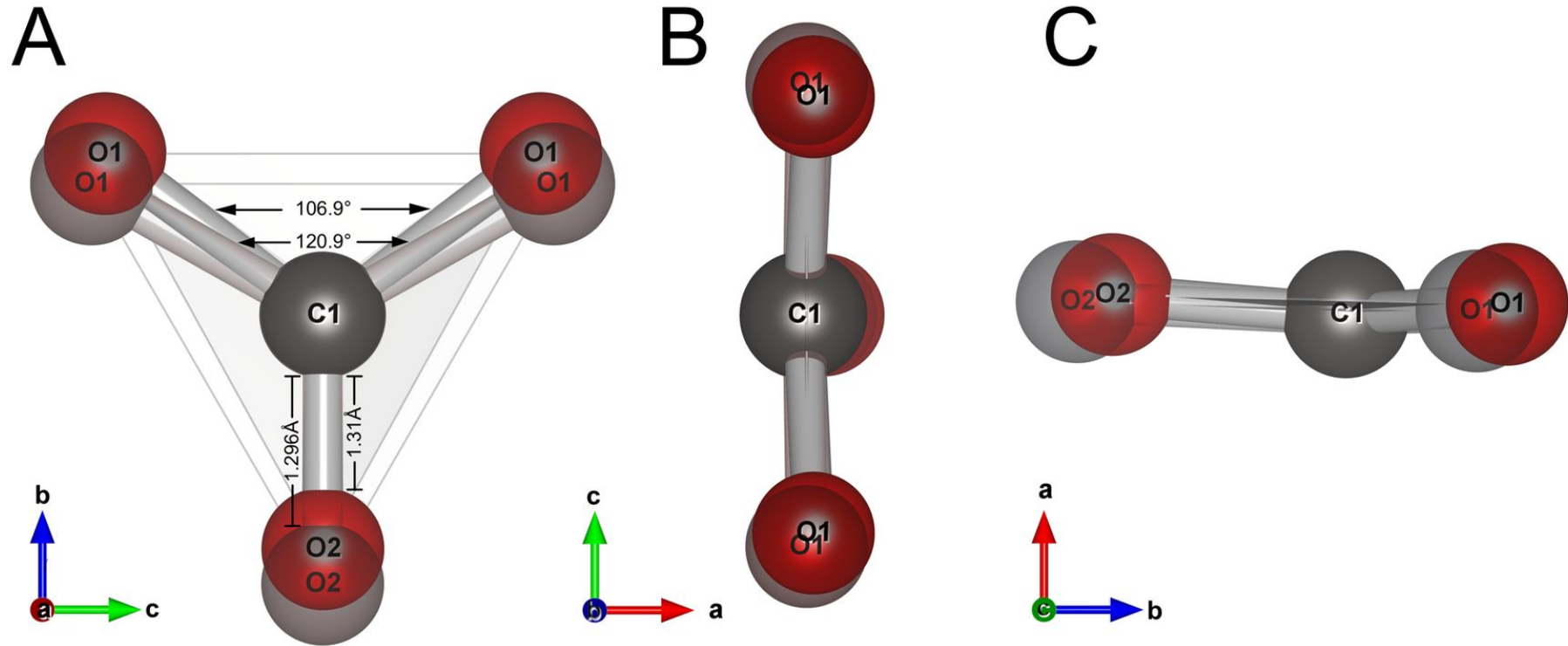
Figure 7
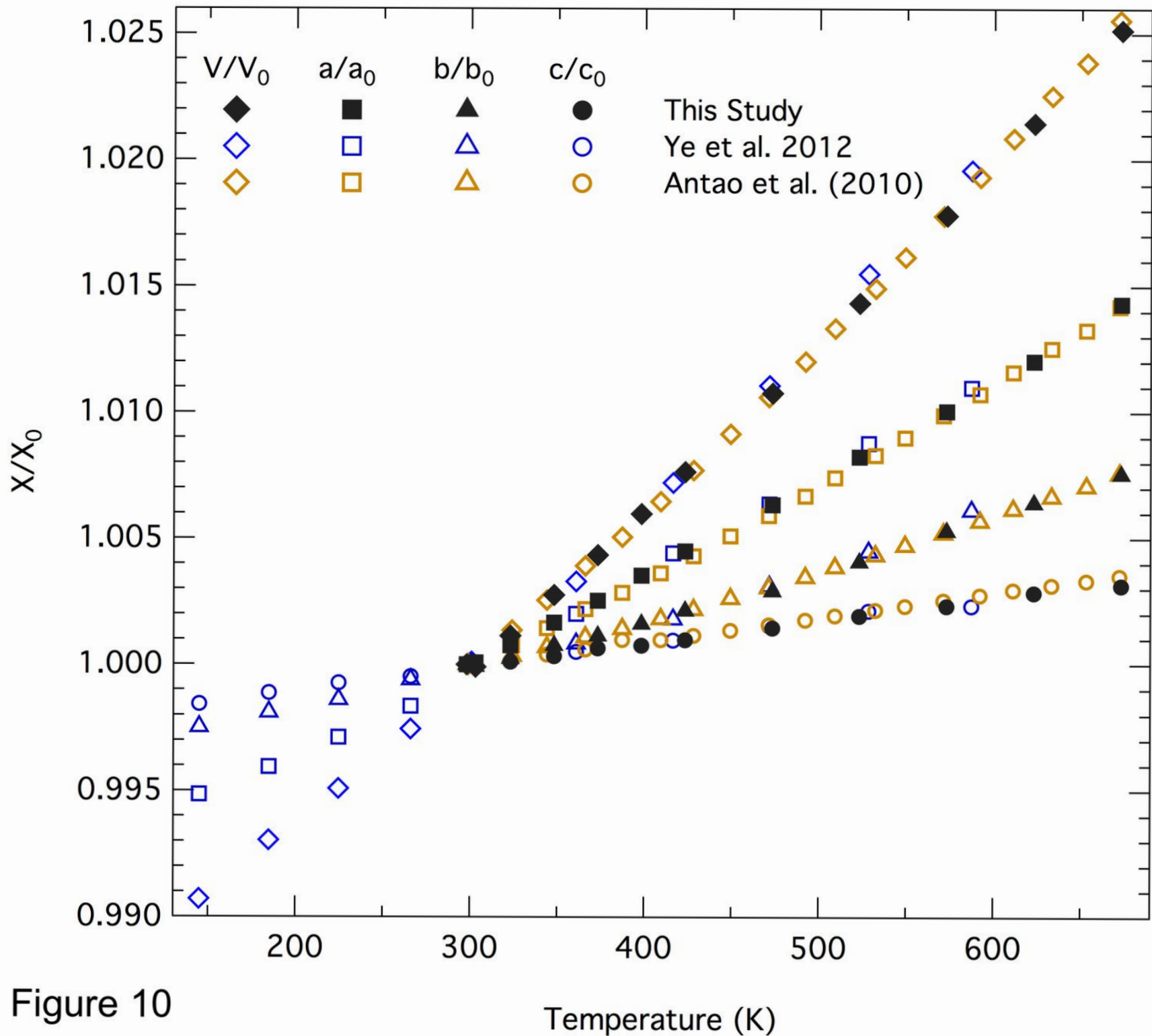
Figure 8

Figure 9

Figure 10

Pressure	*a*	*b*	*c*	Volume
0	5.741(4)	7.97(1)	4.959(4)	226.9(2)
0.57(1)	5.7128(8)	7.942(2)	4.949(4)	224.55(18)
1.2(1)	5.6902(8)	7.922(2)	4.943(4)	222.83(18)
2.28(9)	5.6516(8)	7.886(2)	4.927(4)	219.62(18)
2.96(7)	5.6275(8)	7.865(2)	4.919(4)	217.74(18)
3.8(2)	5.6021(8)	7.847(2)	4.913(4)	215.97(17)
6.0(1)	5.5340(8)	7.789(2)	4.887(4)	210.64(17)
8.0(2)	5.4749(8)	7.744(2)	4.865(4)	206.28(17)
9.9(2)	5.4296(8)	7.711(2)	4.851(4)	203.11(17)
11.6(2)	5.3834(8)	7.676(2)	4.833(4)	199.69(16)
13.8(3)	5.3400(8)	7.652(2)	4.819(4)	196.90(16)
15.7(6)	5.2877(8)	7.616(2)	4.800(4)	193.30(16)
17.5(5)	5.2570(8)	7.598(2)	4.787(4)	191.22(16)
19.5(3)	5.2170(8)	7.580(2)	4.775(4)	188.82(16)
21.1(4)	5.1845(8)	7.558(2)	4.758(4)	186.46(16)
22.8(2)	5.1531(8)	7.543(2)	4.749(4)	184.57(15)
24.03(2)	5.1309(8)	7.538(2)	4.741(4)	183.36(15)
25.38(7)	5.1175(8)	7.528(2)	4.737(4)	182.47(15)
26.7(1)	5.0954(8)	7.514(2)	4.727(4)	180.99(15)
27.9(1)	5.0763(8)	7.504(2)	4.717(4)	179.68(15)
29.1(2)	5.0592(8)	7.495(2)	4.711(4)	178.64(15)
31.4(2)	5.0266(8)	7.475(2)	4.698(4)	176.52(15)
32.9(2)	4.9866(8)	7.502(2)	4.687(4)	175.34(15)
34.8(3)	4.948(2)	7.507(4)	4.663(4)	173.2(2)

T (K)	*a*	*b*	*c*	Volume
298	5.7457(2)	7.9728(3)	4.9638(2)	227.39(2)
303	5.7462(2)	7.9722(3)	4.9634(2)	227.37(2)
323	5.7501(2)	7.9748(3)	4.9644(2)	227.65(2)
348	5.7553(2)	7.9789(3)	4.9655(2)	228.02(2)
373	5.7603(2)	7.982(3)	4.9671(2)	228.38(2)
398	5.7661(2)	7.9858(3)	4.9676(2)	228.75(2)
423	5.7716(2)	7.9899(3)	4.9687(2)	229.13(2)
473	5.7822(2)	7.9961(3)	4.9711(2)	229.84(2)
523	5.7931(2)	8.0054(3)	4.9734(2)	230.65(2)
573	5.8035(2)	8.0151(3)	4.9754(2)	231.44(2)
623	5.8149(2)	8.024(3)	4.978(2)	232.27(2)
673	5.8279(2)	8.033(3)	4.9794(2)	233.11(2)